AD-A212 433 A TWO-STREAM MULTILAYER SPECTRAL RADIATIVE TRANSFER MODEL FOR SEA ICE(U) COLD REGIONS RESEARCH AND ENGINEERING LAB HANOVER NH D K PEROVICH JUL 89 CRREL-89-15 1/1

UNCLASSIFIED F/G 8/12 NL

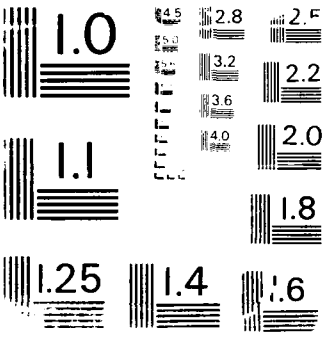
1.0
1.1
1.25
1.4
1.6
1.8
2.0
2.2
2.8
3.2
3.6
4.0
4.5

CRREL REPORT 89-15

US Army Corps of Engineers
Cold Regions Research & Engineering Laboratory

(4)

A two-stream multilayer, spectral radiative transfer model for sea ice

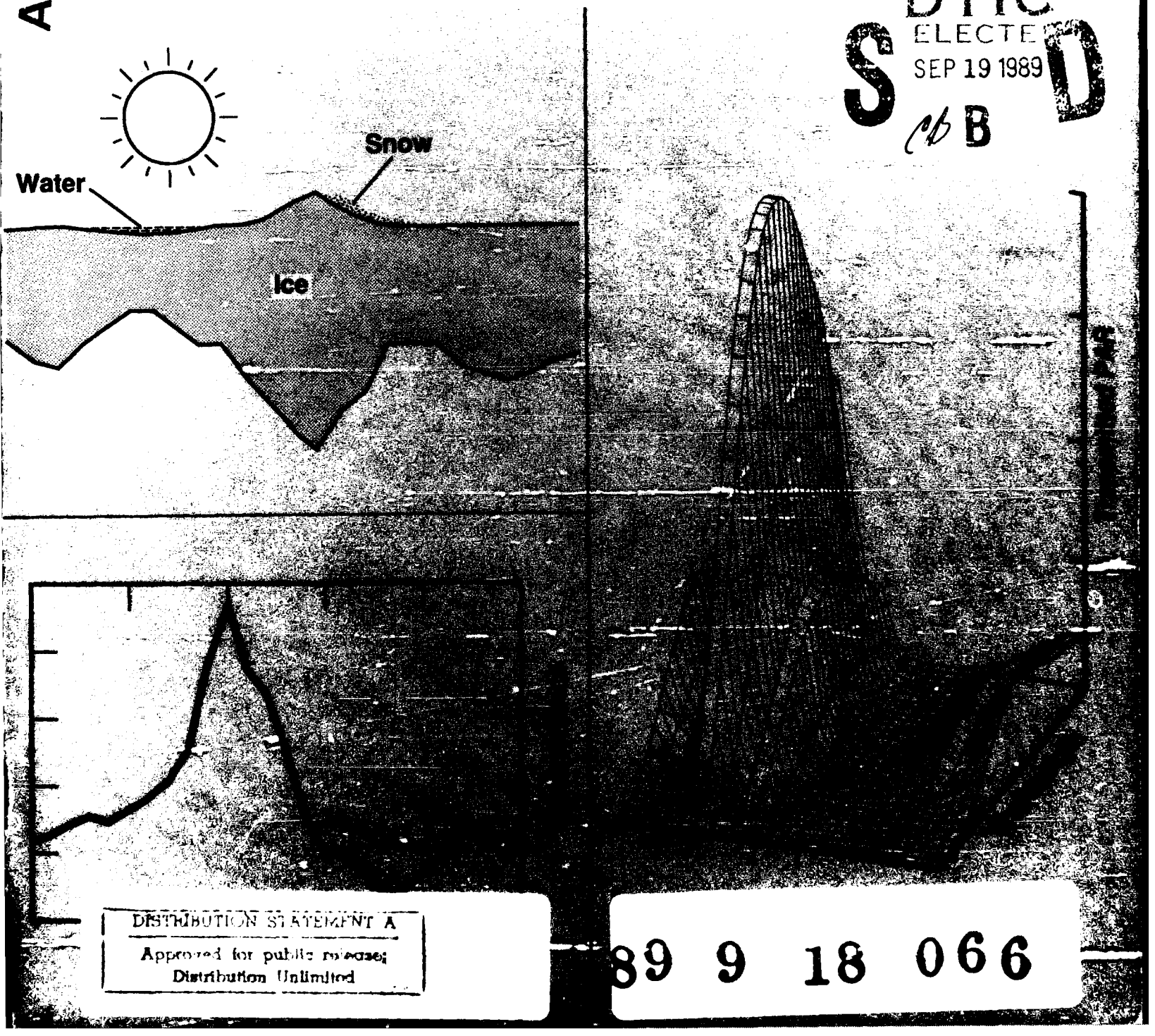

For conversion of SI metric units to U.S./British customary units of measurement consult ASTM Standard E380, Metric Practice Guide, *published by the American Society for Testing and Materials, 1916 Race St., Philadelphia, Pa. 19103.*

CRREL Report 89-15

July 1989

A two-stream multilayer, spectral radiative transfer model for sea ice

Donald K. Perovich

Prepared for
OFFICE OF THE CHIEF OF ENGINEERS

REPORT DOCUMENTATION PAGE

Form Approved
OMB No. 0704-0188
Exp. Date: Jun 30, 1986

1a. REPORT SECURITY CLASSIFICATION: Unclassified	1b. RESTRICTIVE MARKINGS
2a. SECURITY CLASSIFICATION AUTHORITY	3. DISTRIBUTION/AVAILABILITY OF REPORT: Approved for public release; distribution is unlimited.
2b. DECLASSIFICATION/DOWNGRADING SCHEDULE	
4. PERFORMING ORGANIZATION REPORT NUMBER(S): CRREL Report 89-15	5. MONITORING ORGANIZATION REPORT NUMBER(S)
6a. NAME OF PERFORMING ORGANIZATION: U.S. Army Cold Regions Research and Engineering Laboratory; 6b. OFFICE SYMBOL (if applicable): CECRL	7a. NAME OF MONITORING ORGANIZATION: Office of the Chief of Engineers
6c. ADDRESS (City, State, and ZIP Code): Hanover, New Hampshire 03755-1290	7b. ADDRESS (City, State, and ZIP Code): Washington, D.C. 20314-1000
8a. NAME OF FUNDING/SPONSORING ORGANIZATION; 8b. OFFICE SYMBOL (if applicable)	9. PROCUREMENT INSTRUMENT IDENTIFICATION NUMBER
8c. ADDRESS (City, State, and ZIP Code)	10. SOURCE OF FUNDING NUMBERS: PROGRAM ELEMENT NO. 6.1102; PROJECT NO. 4A161102 AT24; TASK NO. SS; WORK UNIT ACCESSION NO. 05

11. TITLE (Include Security Classification)
A Two-Stream, Multilayer, Spectral Radiative Transfer Model for Sea Ice

12. PERSONAL AUTHOR(S)
Perovich, Donald K.

13a. TYPE OF REPORT	13b. TIME COVERED FROM ____ TO ____	14. DATE OF REPORT (Year, Month, Day): July 1989	15. PAGE COUNT: 20

16. SUPPLEMENTARY NOTATION
Additional funding provided by Office of Naval Research N0001488WM24013

17. COSATI CODES: FIELD	GROUP	SUB-GROUP

18. SUBJECT TERMS (Continue on reverse if necessary and identify by block number)
Albedo, Sea ice, Arctic, Shortwave radiation, Radiative transfer

19. ABSTRACT (Continue on reverse if necessary and identify by block number)

The reflection, absorption, and transmission of light at visible and near-infrared wavelengths is important for a number of geophysical problems. Light reflection is an important parameter in remote sensing studies, absorption is significant to ice thermodynamics, and transmission strongly influences biological activity in and under the ice. The focus of this report is on the reflection and transmission of light by spatially inhomogeneous and temporally varying sea ice covers. This is investigated using a two-stream, multilayer radiative transfer model in the wavelength region from 400 to 1000 nm. The model is computationally simple and utilizes the available experimental data on the optical properties of sea ice. The ice cover is characterized as a layered medium composed of selections from nine distinct snow and ice types. Three case studies are presented illustrating values of spectral albedo, transmittance, and transmitted photosynthetically active radiation (PAR) for 1) a spatially inhomogeneous ice cover, 2) a uniform ice cover as it undergoes a melt cycle, and 3) a temporally changing spatially variable ice cover. The importance of thickness and surface conditions on the reflected and transmitted radiation fields is demonstrated.

20. DISTRIBUTION/AVAILABILITY OF ABSTRACT	21. ABSTRACT SECURITY CLASSIFICATION
☒ UNCLASSIFIED/UNLIMITED ☐ SAME AS RPT ☐ DTIC USERS	Unclassified

22a. NAME OF RESPONSIBLE INDIVIDUAL	22b. TELEPHONE (Include Area Code)	22c. OFFICE SYMBOL
Donald K. Perovich	603-646-4100	CECRL-RS

DD FORM 1473, 84 MAR — 83 APR edition may be used until exhausted. All other editions are obsolete.

PREFACE

This report was prepared by Dr. Donald Perovich, Geophysicist, of the Snow and Ice Branch, Research Division, U.S. Army Cold Regions Research and Engineering Laboratory. Funding for this research was provided by DA Project 4A161102AT24, *Research in Snow, Ice and Frozen Ground*, Task SS, Work Unit 05, *Electromagnetic and Radiative Characteristics of Snow, Ice and Frozen Ground*, and by the Office of Naval Research, Contract N0001488WM24013.

The author thanks Walter Tucker and Gary Koh of CRREL for technically reviewing this report and Kathleen Jones for mathematical expertise.

CONTENTS

ILLUSTRATIONS

Figure

TABLES

Table

A Two-Stream, Multilayer, Spectral Radiative Transfer Model for Sea Ice

DONALD K. PEROVICH

INTRODUCTION

The reflection, absorption, and transmission of shortwave radiation by snow and ice covers are significant in a variety of geophysical problems. Spectral reflectance is important in the interpretation of imagery from remote sensing instruments operating at visible and near-infrared wavelengths. Maykut and Untersteiner (1971), Grenfell and Maykut (1977), and Maykut and Perovich (1987) have established the critical role played by shortwave radiation in the heat balance of a sea ice cover. Primary productivity and other biological activity under a sea ice cover are strongly affected by the amount and spectral composition of transmitted light (SooHoo et al. 1987).

Because of this established importance, there is a substantial data base of optical measurements of reflected and transmitted light in snow and ice covers. Observational data on the optical properties of snow and of sea ice are reviewed in Warren (1982) and Perovich et al. (1986), respectively. These observations indicate that understanding radiative transfer in snow and ice is considerably complicated by the large temporal and spatial variability in the physical, and therefore optical, properties of the medium. For example, observations indicate that as a snow cover ages, and metamorphism increases its grain size, there is a decrease in albedo (Grenfell and Perovich 1981). The physical structure of sea ice can be even more complex, with vertical variations in vapor inclusions, ice temperature, salinity, and brine volume. Observations have demonstrated that the optical properties of sea ice depend on the ice temperature, brine volume (Perovich and Grenfell 1981) and surface conditions (Grenfell and Maykut 1977).

This complexity necessitates use of theoretical models both to interpret and to extrapolate the observational data. Over the years several different models have been formulated to describe radiative transfer in snow and ice. Warren (1982) provides an excellent summary of radiative transfer models that have been applied to snow. One, in particular, developed by Wiscombe and Warren (1980), has proved very useful for snow applications. Mullen and Warren (1988) used a modified delta-Eddington approach to model spectral albedos of lake ice. Perovich and Grenfell (1982) and Grenfell (1983) adapted the discrete ordinates method of Chandrasekhar (1960) to sea ice. The Dunkle and Bevans (1956) model, based on Schuster (1905), calculates the upwelling and downwelling irradiance in a snowpack. The model was used by Grenfell and Maykut (1977), Grenfell (1979), and Perovich and Grenfell (1981) to interpret field and laboratory measurements of the optical properties of sea ice.

These models all have features that both recommend and limit them for particular applications. Often there are tradeoffs between detailed physics and computational simplicity. In this report we will develop and present a two-stream, multilayer model of radiative transfer at visible and near-infrared wavelengths. While this discussion is directed specifically toward a sea ice cover, the formulation is sufficiently general to be easily adapted to other translucent media such as lake ice, river ice, or turbid water. The major limitation of this model

lies in its casual treatment of the physics of scattering, in particular in its assumption of isotropic scattering and the lack of information concerning the angular distribution of the radiation field. However, since our interest is in irradiance, the radiance integrated over angle, this is not a major difficulty. The model has three primary advantages. Computationally it is simple and fast, avoiding the numerical difficulties of more advanced methods. Thus it can be run quickly on a personal computer, allowing a wide range of cases to be investigated easily. In addition, this two-stream model can directly exploit the large observational data base of sea ice optical properties compiled by Grenfell and Maykut (1977), Grenfell (1979), and Perovich and Grenfell (1981). Finally, only a qualitative depiction of the ice structure (blue ice, white ice, melting ice) is needed, rather than the detailed statistical description of the scattering inhomogeneities demanded by more sophisticated models.

THEORY

The model is of two streams in that it calculates a downwelling ($F_\downarrow$) and an upwelling ($F_\uparrow$) irradiance in the medium. The irradiance is defined as the total energy per unit area per unit time (W/m^2) incident on a horizontal plane from the lower ($F_\uparrow$) and upper ($F_\downarrow$) hemispheres. In the medium each layer is considered to be plane parallel, i.e. homogeneous in z and infinite in extent in x and y. The optical properties of a layer are defined in terms of wavelength-dependent scattering (r_λ) and extinction (κ_λ) coefficients. The downwelling and upwelling irradiances are governed by the coupled first-order differential equations:

$dF_\downarrow(z,\lambda) =$	$-k_\lambda F_\downarrow(z,\lambda)dz$	$-r_\lambda F_\downarrow(z,\lambda)dz$	$+r_\lambda F_\uparrow(z,\lambda)dz$	(1)
Change in downwelling	Loss to absorption	Scattering loss from downwelling	Scattering gain from upwelling	
$dF_\uparrow(z,\lambda) =$	$k_\lambda F_\uparrow(z,\lambda)dz$	$-r_\lambda F_\downarrow(z,\lambda)dz$	$+r_\lambda F_\uparrow(z,\lambda)dz$	(2)
Change in upwelling	Loss to absorption	Scattering gain from downwelling	Scattering loss from upwelling	

where z is the depth within the medium (increasing downward) and λ is the wavelength of the light. Scattering (r_λ) and absorption (k_λ) are treated through wavelength-dependent coefficients. Together the scattering and absorption coefficients define the extinction coefficient κ_λ where $\kappa_\lambda = \sqrt{(k_\lambda^2 + 2k_\lambda r_\lambda)}$. If there is no scattering eq 1 reduces to

$$dF_\downarrow(z,\lambda) = -k_\lambda F_\downarrow(z,\lambda)dz,$$

which when integrated yields the familiar Bouguer-Lambert law

$$F_\downarrow(z,\lambda) \propto e^{-k_\lambda z}.$$

Equation 2 reduces to $F_\uparrow(z,\lambda) = 0$ for the no-scattering case. Equations 1 and 2 can be reformulated as uncoupled second-order differential equations (see App. A for details) with general solutions of

$$F_\downarrow(z,\lambda) = A \sinh(\kappa_\lambda z) + B \cosh(\kappa_\lambda z) \tag{4}$$

$$F_\uparrow(z,\lambda) = C \sinh(\kappa_\lambda z) + D \cosh(\kappa_\lambda z). \tag{5}$$

This method converges to a simple exponential decay for optically thick media, but as Grenfell (1979) points out it offers substantial improvements in accuracy over exponential decay for optically thin cases.

The geometry of the multilayer model is schematically illustrated in Figure 1. We consider N layers, with each layer i having thickness H_i and optical properties defined by the constants $k_{\lambda i}$ and $r_{\lambda i}$. We assume that there is no specular reflection at the interfaces between layers. To specify the solution to eq 4 and 5 for a layer it is necessary to determine the four constants A, B, C, and D. Hence $4N$ equations are needed to solve an N-layer system.

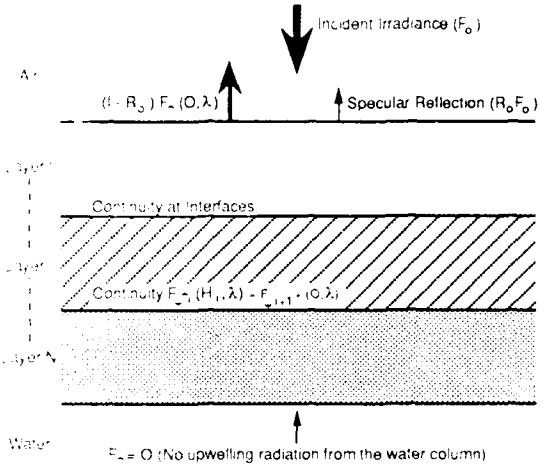

Figure 1. Schematic of two-stream, n-layer model.

Two equations are provided by the surface and bottom boundary conditions. At the surface we have

$$F_\downarrow(0,\lambda) = (1-R_0)F_0 + R_0F_\uparrow(0,\lambda), \tag{6}$$

where F_0 is the incident solar irradiance and R_0 is the specular reflection at the surface. At the bottom boundary we assume that there is no specular reflection and there is no upwelling from below, yielding a boundary condition of

$$F_\downarrow(H_N,\lambda) = 0. \tag{7}$$

We require continuity at the interfaces between layers. These matching conditions provide $2(N-1)$ equations of the form

$$F_\uparrow(H_i,\lambda) = F_{\uparrow i+1}(0,\lambda) \tag{8}$$

$$F_\downarrow(H_i,\lambda) = F_{\downarrow i+1}(0,\lambda). \tag{9}$$

In eq 6 through 9 the two subscripts on F define the direction ($\downarrow$,$\uparrow$) and the layer number i, and H_i is the layer thickness. The remaining $2N$ equations are obtained by applying the differential equations 1 and 2 at the top of every layer. This is done at the top of the layer, since $z = 0$ simplifies the resulting equations.

Substituting the general solutions (eq 4 and 5) into these $4N$ equations yields the following system of equations for each wavelength,

$(1 - R_0)F_0 + R_0D_1 = B_1$	(top boundary condition)
$C_N \sinh(\kappa_N H_N) + D_N \cosh(\kappa_N H_N) = 0$	(bottom boundary condition)
$A_i \sinh(\kappa_i H_i) + B_i \cosh(\kappa_i H_i) = B_{i+1}$	(N–1 matching conditions, $i = 1, N-1$)
$C_i \sinh(\kappa_i H_i) + D_i \cosh(\kappa_i H_i) = D_{i+1}$	(N–1 matching conditions, $i = 1, N-1$)
$A_i\kappa_i + B_i(k_i + r_i) - D_i r_i = 0$	(N equations for $i = 1,N$)
$B_i r_i + C_i\kappa_i - (k_i + r_i)D_i = 0$	(N equations for $i = 1,N$).

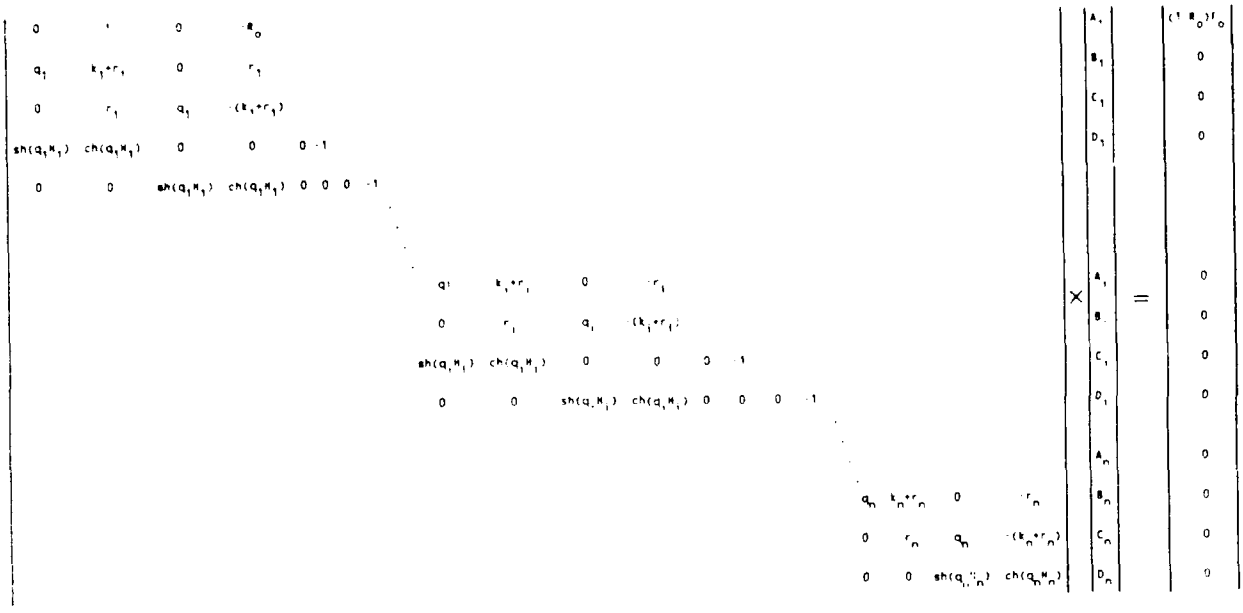

Figure 2. Matrix representing system of equations for two-stream, n-layer model. ch *designates a hyperbolic cosine and* sh *denotes a hyperbolic sine.*

Figure 2 presents the system of equations for an N-layer medium in matrix form. Once the system is solved and values of A_1, B_1, C_1 and D_1 determined, the upwelling and downwelling irradiance can be calculated anywhere in the medium. When computing irradiances the depth z is with respect to the layer rather than the entire medium. This convention improves the numerical accuracy of the solution.

Two parameters of particular interest are the spectral albedo (α_λ) and the transmittance (T_λ). The spectral albedo is the ratio of the reflected and incident irradiance, or

$$\alpha_\lambda = (R_0 F_{0\lambda} + D_1) \; / \; F_{0\lambda}.$$

The spectral transmittance is the ratio of the transmitted and the incident irradiance, or

$$T_\lambda = [A_\lambda \sinh(\kappa_\lambda H_\lambda) + B_\lambda \cosh(\kappa_\lambda H_\lambda)]/F_{0\lambda}.$$

These spectral values can be integrated over wavelength to give bulk values of albedo (α_B)

$$\alpha_B = \int \alpha_\lambda F_{0\lambda}(\lambda) d_\lambda / \int F_{0\lambda}(\lambda)\, d\lambda$$

and transmittance (T_B)

$$T_B = \int T_\lambda F_{0\lambda}(\lambda)\, d\lambda / \int F_{0\lambda}(\lambda)\, d\lambda.$$

For biological purposes, the downwelling spectral irradiance at the underside of the ice is of considerable interest. Since it is the number of photons of particular wavelengths that controls biological activity, irradiance is presented in terms of photons of wavelength λ per unit area per time, rather than the more familiar units of W/m^2 (SooHoo et al. 1987). The basic unit for this is an einstein (E), which is equal to the energy of a mole of photons of wavelength λ. More precisely an einstein is defined as

$$E_\lambda = nhc/\lambda,$$

where n = Avogadro's number (6.025×10^{23}), h = Planck's constant (6.625×10^{-34} J·s), and c

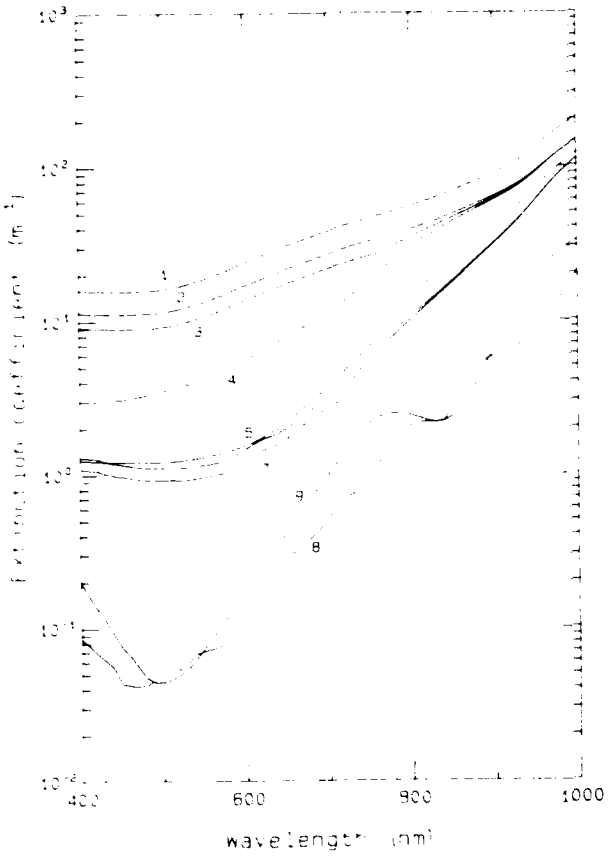

Figure 3. Spectral extinction coefficients for nine medium types used in the sea ice radiative transfer model; 1) dry snow, 2) melting snow, 3) ice colder than the eutectic point, 4) surface scattering layer of white ice, 5) interior portion of white ice, 6) cold blue ice, 7) melting blue ice, 8) bubble- free fresh ice, and 9) clear arctic water.

= speed of light (3×10^{17} nm/s). The total photosynthetically active radiation (PAR) is equal to the irradiance (units of mE/m^2 s) integrated from 400 to 700 nm.

THE SEA ICE MODEL

To illustrate the efficacy of the multilayer formulation, we now apply it to the specific case of a sea ice cover. The input parameters needed for the model are spectral scattering and extinction coefficients for each medium type considered, layer thickness, and optionally the incident spectral irradiance.

For the sea ice model nine medium types were included: 1) cold dry snow, 2) melting wet snow, 3) ice colder than the eutectic point, 4) surface scattering layer of white ice, 5) the interior portion of white ice, 6) cold blue ice, 7) melting blue ice, 8) bubble-free fresh ice, and 9) clear arctic water. Spectral extinction coefficients for these nine types are plotted in Figure 3. The extinction coefficients for ice types 1, 4, 5, and 7 came directly from Grenfell and Maykut (1977), type 3 from Perovich (1979), type 8 from Grenfell and Perovich (1981) and type 9 from Grenfell (1979) (Smith and Baker 1981). The melting wet snow and cold blue ice values were obtained by adjusting the scattering coefficients for cold dry snow and melting blue ice in order to reproduce spectral albedos reported in Grenfell and Perovich (1984) for melting snow and cold blue ice. Extinction coefficients beyond 800 nm have been extrapolated from observations and are somewhat suspect. Because of experimental errors due to light leakage and lack of spectral resolution, extinction coefficients at longer wavelengths are quite possibly larger than reported here.

Values for the scattering coefficients were not explicitly reported in any of the above papers, though spectral albedos were presented. Therefore we determined scattering coefficients by entering the extinction coefficients from Figure 3 into the two-stream model and varying the scattering coefficient to reproduce the reported albedos. In the visible and near infrared, the scattering inhomogeneities are much larger than the wavelength, and the scattering coefficient does not vary with wavelength (Grenfell 1983, Bohren and Huffman 1983). The bubble-free ice and clear arctic water cases were assumed to be purely absorbing media. Scattering coefficients (Table 1) varied from zero for bubble-free fresh ice and arctic water to 800 m^{-1} for cold dry snow.

Table 1. Scattering coefficients (m^{-1}) for nine medium types.

Medium	*Scattering coefficient*
Cold dry snow	800
Melting wet snow	160
Ice below eutectic	160
White ice scattering	120
White ice interior	2.5
Cold blue ice	1.8
Melting blue ice	1.2
Bubble-free ice	0.0
Clear arctic water	0.0

Note: The scattering coefficients are constant with wavelength.

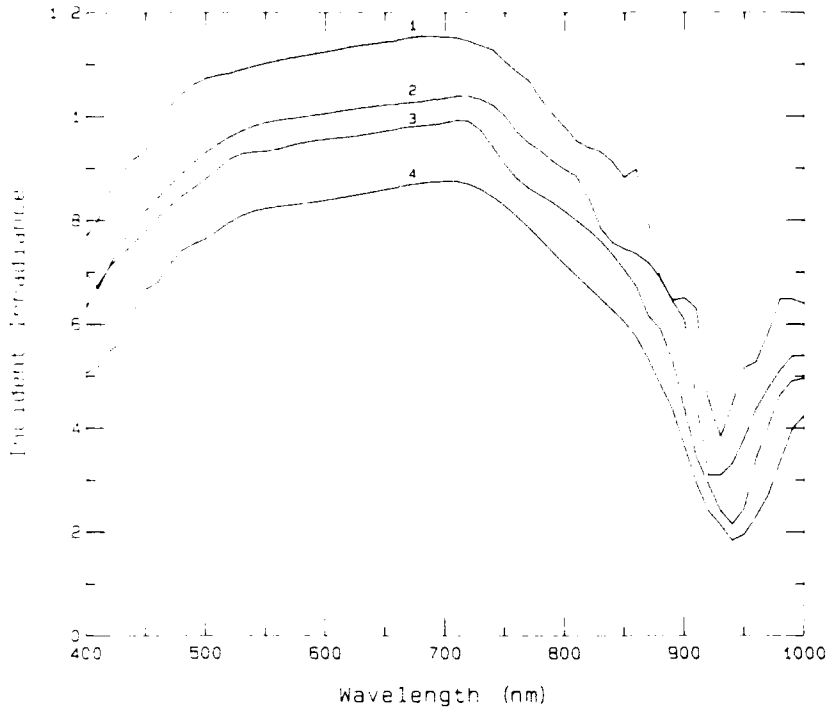

Figure 4. Normalized values of spectral incident irradiance under arctic conditions of 1) clear skies, 2) light clouds, solar disk visible, 3) cloudy, solar disk barely visible, and 4) heavy overcast, solar disk not visible (from Grenfell and Perovich 1984). These values are multiplied by wavelength integrated incident irradiance (400–2400 nm) to obtain spectral incident irradiances.

Spectral albedos and transmittances do not depend on the spectral composition of the incident radiation, so if these are the parameters of interest $F_0(\lambda)$ is not needed. However, there are other situations, particularly in biological applications, where absolute values of upwelling or downwelling irradiance are desired. In these cases $F_0(\lambda)$ must be specified. Representative arctic spectra of incident solar irradiances measured at Point Barrow, Alaska, were incorporated into the model (Grenfell and Perovich 1984). The sky conditions for the four curves presented in Figure 4 were 1) clear skies, 2) light clouds, solar disk clearly visible, 3) cloudy, solar disk barely visible, and 4) heavy overcast solar disk not visible. The plotted values are normalized and represent the fraction per micrometer of the total incident irradiance and thus must be multiplied by the total incident irradiance from 400–2400 nm. One somewhat disturbing feature of the curves is that the maxima are about 700 nm, which is contrary to other observations (Gast 1960) and to our belief of a yellow sun. In actuality the maxima are not indicative of a reddening of the sun, but rather are a manifestation of 10–15% uncertainties in absolute spectral irradiances.* This illustrates a need for more precise measurements of incident spectral irradiance under arctic conditions.

Both the albedo and the upwelling irradiance at the surface can have a specular reflection component (R_0). This is strictly a surface phenomenon arising from index of refraction differences at the interface between two media. The indices of refraction of ice and water are so close, 1.31 and 1.33 respectively, that R_0 at the bottom ice-water boundary is assumed to be zero. However since air has an index of refraction of 1, R_0 at the surface is not negligible. Under diffuse sky conditions, R_0 for air/ice or air/water will be 0.05 (Perovich and Grenfell 1982). The dry and wet snow types have a rough granular surface and we cannot distinguish specular reflection from scattering, so we assume $R_0 = 0$.

* Personal communication with T.C. Grenfell, University of Washington, 1988.

A computer program, utilizing the solution presented in the theory section, was written to calculate the upwelling and downwelling irradiances and associated parameters for an arbitrary medium consisting of up to 15 distinct layers. By inputting the reflection and extinction coefficients for the nine media types, the general model can be customized for sea ice. The model allows selection of the number, type, and thickness of layers, along with the incident shortwave irradiance, sky conditions and spectral range of interest. Output parameters include spectral values of surface upwelling irradiance, bottom downwelling irradiance, albedo, transmittance, and PAR, and wavelength integrated values of bulk albedo, transmittance, transmitted flux, and PAR. Because of the relative simplicity of the model, the solution can be quickly calculated on a personal computer.

APPLICATIONS OF THE MODEL

We shall demonstrate the utility of the radiative transfer model by applying it to three distinct cases: 1) obtaining a two-dimensional spatial picture of the transmitted radiation field through a cold ice cover which varies in X and Y, 2) monitoring temporal changes in light transmission through melting ice, and 3) determining combined spatial and temporal variations in light transmission. The major focus of these three examples will be on the transmitted spectral radiation, with some attention paid to spectral albedos. In addition to showing the capabilities of the model, the examples have been selected to illustrate the effects of variations in ice thickness, snow cover, surface conditions, and ice types on the optical properties.

Spatial variations

Tucker* used a hot water drill to perform a detailed mapping of ice and snow thickness on several floes in the Beaufort Sea. Figure 5 summarizes the snow and ice thickness data from one of these floes, where 121 ice thicknesses were measured for a 100- × 100-m section using a 10-m grid. This area consisted of deformed multiyear ice with a primarily columnar crystal texture. Since the observations were made in April, the snow cover was cold and dry, and the ice was cold but not below the eutectic point. Ice thicknesses ranged from 1.8 to 6.5 m with a mean of 3.01 m, while snow thicknesses varied from 0 to 0.34 m with a mean of 0.07 m.

The ice cover is assumed to be relatively homogeneous, consisting of interior white ice. Thus variations in light transmission are primarily due to differences in snow and ice thickness. The two-dimensional spatial distribution of transmitted light at 470 nm is plotted in Figure 6. The fraction transmitted spans over 5 orders of magnitude from 0.88×10^{-6} to 0.63×10^{-1}. Features in this plot do not necessarily correlate with the ice thickness topography. The peaks in transmitted light correspond to areas of bare ice, while minimum values occur where the snow was the deepest. Distributions at other wavelengths are similar in shape to Figure 6, but have reduced magnitudes.

The question arises whether this detailed spatial computation results in a better representation of light reflection and transmission for this area. To address this issue, spectral albedos and transmittances were calculated for the 121 points on Tucker's thickness grid. These values were then averaged to generate an areal estimate for the region and are plotted as curve 1 in Figures 7a and 7b. For comparison another areal estimate was computed more simplistically by first determining the mean snow and ice thicknesses and then calculating spectral values for this single case (curve 2). As curves 1 and 2 indicate, there is a significant disparity between these two methods with the simplistic method yielding albedos roughly 0.05 higher and transmittances nearly an order of magnitude lower than the more detailed analysis. Of course this is not surprising since radiative transfer processes are more exponential than linear with depth. As a direct consequence of this, the actual areal averaged transmittance will always be greater than or equal to values computed by using mean snow and ice

* Personal communication with Walter B. Tucker III, CRREL, 1988.

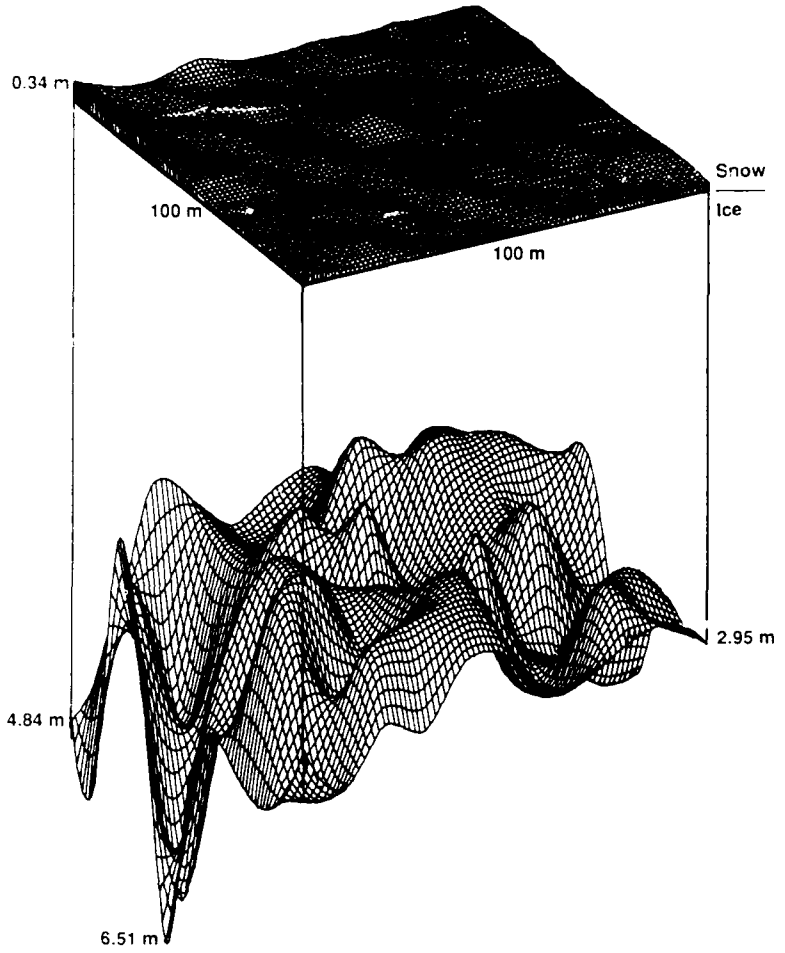

Figure 5. Snow and ice thickness data from Tucker (personal communication, 1988). The bottom and top surfaces represent the thicknesses of the ice and the snow cover respectively. The thickness data were taken at 10-m spacings on a 100- × 100-m grid.

thicknesses for the area. The difference is particularly pronounced for cases such as this in which part of the area is snow free.

Temporal variations

Even a spatially uniform ice sheet can be optically complex when it is undergoing temporal changes. From an optical perspective the most dramatic changes occur in the early portion of the melt season as the ice cover evolves from an opaque snow-covered medium to translucent bare or ponded ice. This transition is of particular interest biologically, since some of the organisms living in and under the ice are light limited and the removal of the snow cover governs the onset of biological activity. To illustrate this point we will examine the optical evolution of a topographically simple ice sheet during the early melt season. In the spring of 1982, Mould Bay fiord (Prince Patrick Island in the Canadian Archipelago) was covered by 2.2 m of flat, undeformed, first-year ice overlaid by 0.30 m of snow (Perovich 1983). The snow melted quickly between 21 and 25 June, transforming the entire ice sheet into a melt pond for a few days, until it isostatically readjusted, leaving predominantly melting blue ice and shallow melt ponds, with some patches of drained white ice. These changes in surface conditions are illustrated in Figure 8. By 10 July the ice had thinned to 1.46 m, with most of the melting occurring during July. Table 2 summarizes ice thickness, snow depth, pond depth,

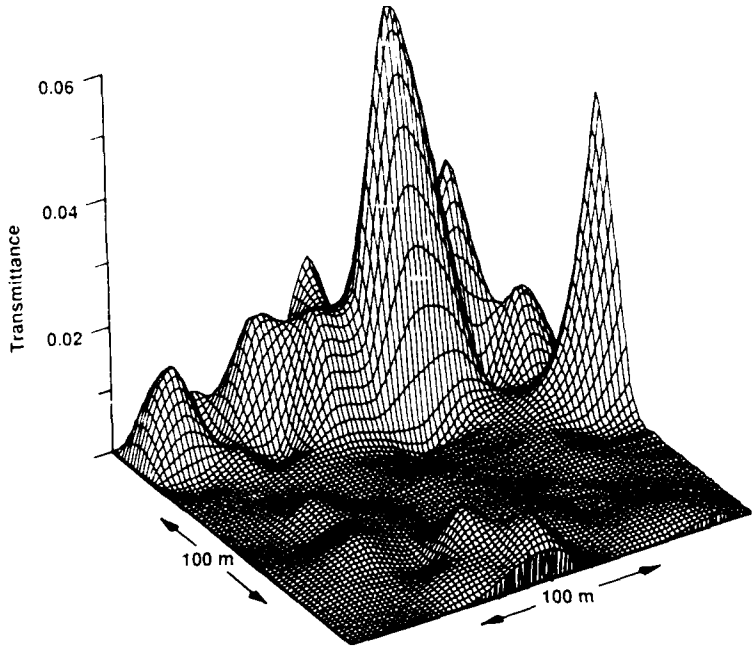

Figure 6. Spatial distribution of light transmittance at 470 nm for ice and snow conditions of Figure 5.

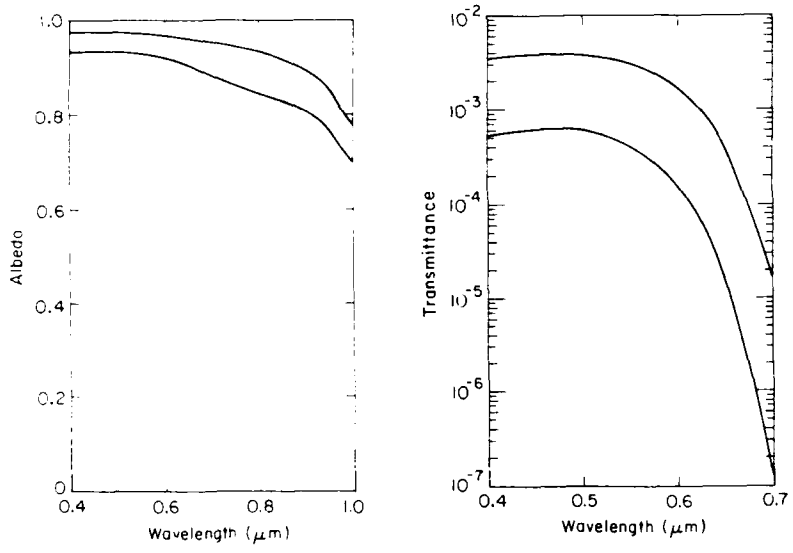

Figure 7. Areally averaged values of spectral albedo and transmittance for ice cover of Figure 5. Curve 1 is the average of the albedos and transmittances computed for the 121 grid points. In curve 2 the average snow and ice thicknesses of the grid were determined; then using these average thicknesses the spectral albedos and transmittances were calculated.

incident shortwave irradiance, and cloud cover for 20 June to 10 July 1982. With these data as input, the radiative transfer model was run for each day.

In Figure 9 albedo is plotted as a function of wavelength and time. The first decrease in albedo occurred on 21 June when the snow began to melt. This drop was somewhat greater at longer wavelengths. There was a precipitous drop three days later when the snow melted and the surface became completely covered by melt ponds. After this point spectral albedos were fairly constant, with some small variations due to changes in pond depths.

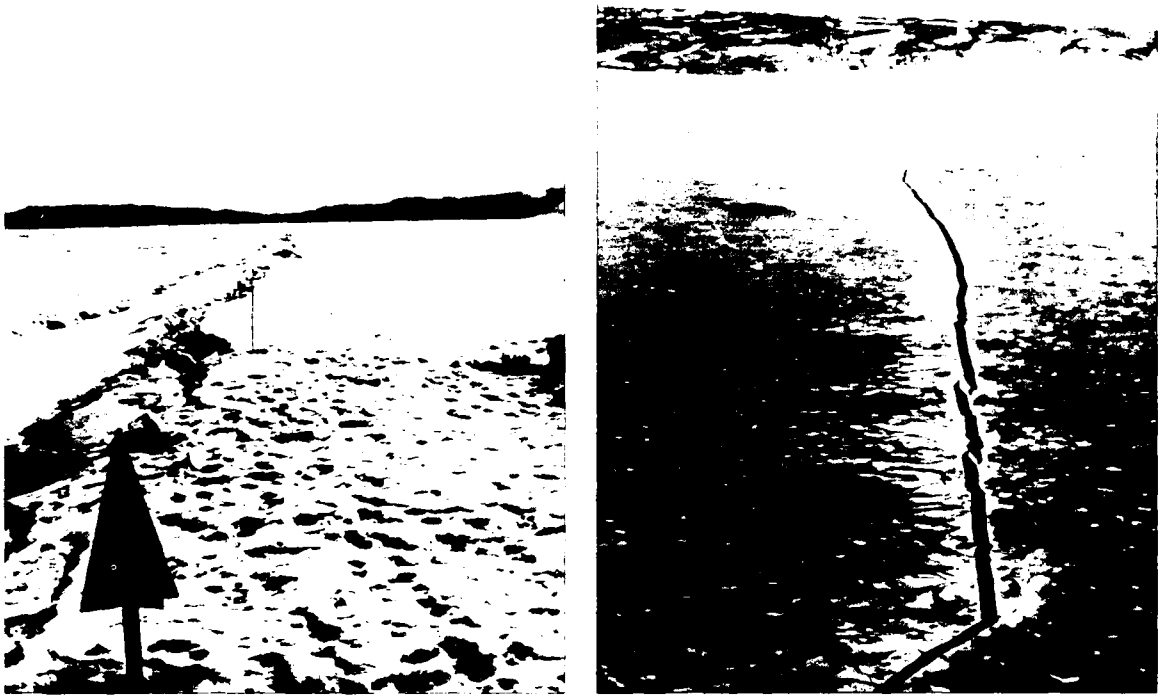

a. 21 June, melting snow. *b. 2 July, heavily ponded.*

Figure 8. Photographs illustrating surface conditions on Mould Bay ice cover.

Table 2. Environmental conditions for Mould Bay ice cover.

Date (1982)	*Ice thickness (m)*	*Surface conditions (m)*	*Incident shortwave (W/m^2)*	*Cloud conditions*
20 June	2.22	0.30 DS	310	Heavy overcast, solar disk not visible
21 June	2.22	0.30 MS	316	Light clouds, solar disk clearly visible
22 June	2.22	0.20 MS	357	Clear skies
23 June	2.22	0.10 MS	352	Clear skies
24 June	2.22	0.10 MP	209	Heavy overcast, solar disk not visible
25 June	2.20	0.20 MP	199	Heavy overcast, solar disk not visible
26 June	2.18	0.10 MP	178	Heavy overcast, solar disk not visible
27 June	2.16	0.05 MP	353	Light clouds, solar disk clearly visible
28 June	2.14	0.05 MP	235	Cloudy, solar disk barely visible
29 June	2.12	0.05 MP	332	Clear skies
30 June	2.10	0.10 MP	326	Clear skies
1 July	2.03	0.05 MP	231	Cloudy, solar disk barely visible
2 July	1.96	0.10 MP	337	Clear skies
3 July	1.89	0.05 MP	228	Cloudy, solar disk barely visible
4 July	1.83	0.05 MP	126	Heavy overcast, solar disk not visible
5 July	1.76	0.05 MP	170	Heavy overcast, solar disk not visible
6 July	1.69	0.05 MP	241	Cloudy, solar disk barely visible
7 July	1.62	0.05 MP	313	Light clouds, solar disk clearly visible
8 July	1.56	0.05 MP	335	Clear skies
9 July	1.53	0.05 MP	312	Clear skies
10 July	1.49	0.05 MP	312	Clear skies

Note: The surface conditions give the thickness and type of surface layer where DS is dry snow, MS is melting snow, and MP is melt pond.

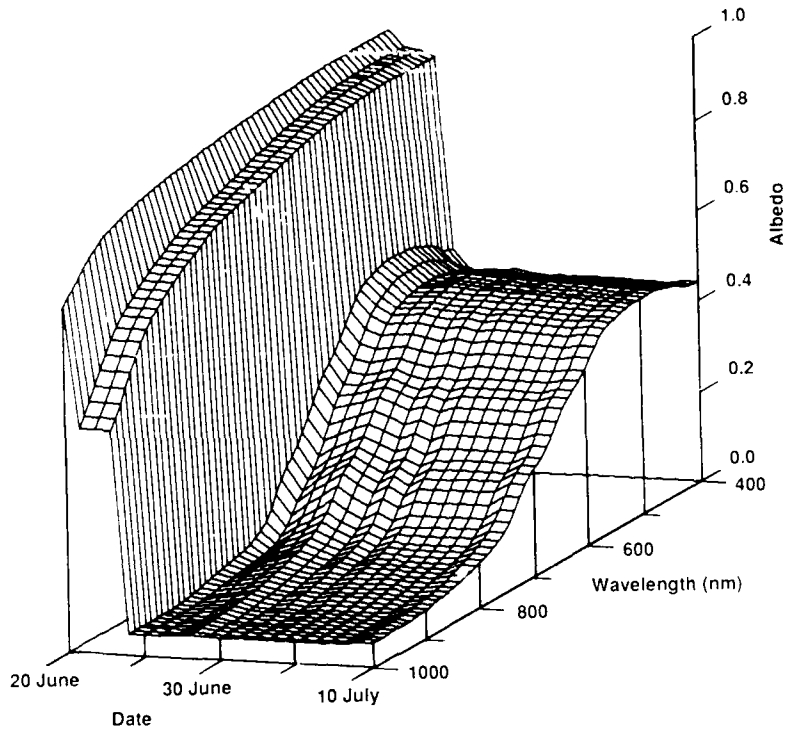

Figure 9. Temporal evolution of spectral albedo for the Mould Bay ice cover.

Spectral values of transmitted PAR for the same time period are plotted in Figure 10. The snow cover was still present for the first few days and an insignificant amount of light was transmitted. Once the snow melted and ponds formed, PAR values increased sharply, especially at shorter wavelengths. As the ice thinned over the next two weeks there was a general upward trend in transmitted PAR. This upward trend increased in July as the ice thinning accelerated. The occasional small decrease occurred on cloudy days with low incident solar irradiance. The spectral peak of transmitted PAR was at 530 nm. Total PAR displayed a similar behavior, increasing by more than an order of magnitude as the the snow cover began to melt (20–21 June), then sharply by a factor of 100 as the snow completely melted and the ice surface became flooded (21–24 June), and finally a gradual 10-fold increase as melting progressed and the ice cover thinned (25 June–10 July).

Spatial and temporal variations

In the more dynamically active regions of the Arctic simple undeformed ice sheets, as found in Mould Bay, are quite scarce. More common is an ice cover with some surface topography, perhaps a ridge, a few hummocks, a low area or two, and typically a variable snow cover. In such a case, spatial variations in ice conditions can further complicate the temporal evolution of the transmitted radiation field.

To illustrate the combined effects of spatial and temporal variations let us examine three sites that were monitored from 20 June to 7 July during the 1984 Marginal Ice Zone Experiment (Maykut and Perovich 1985). These sites were all within 5 m of one another along a small pressure ridge. Site 1 was on the side of the ridge where the snow cover was deepest and had snow present through 7 July. Site 2 was at the top of the ridge, where the surface was snow free, though covered with 0.03 m of melting granular white ice throughout the experiment. Site 3 was initially covered by 0.21 m of snow, which melted by 3 July. A melt pond formed at this site, reaching a depth of 0.20 m by 7 July. Snow and ice thicknesses, surface conditions and the incident radiation field for these three sites are summarized in Table 3.

Spectral albedos for the three sites are summarized in Figure 11. Surface conditions at site

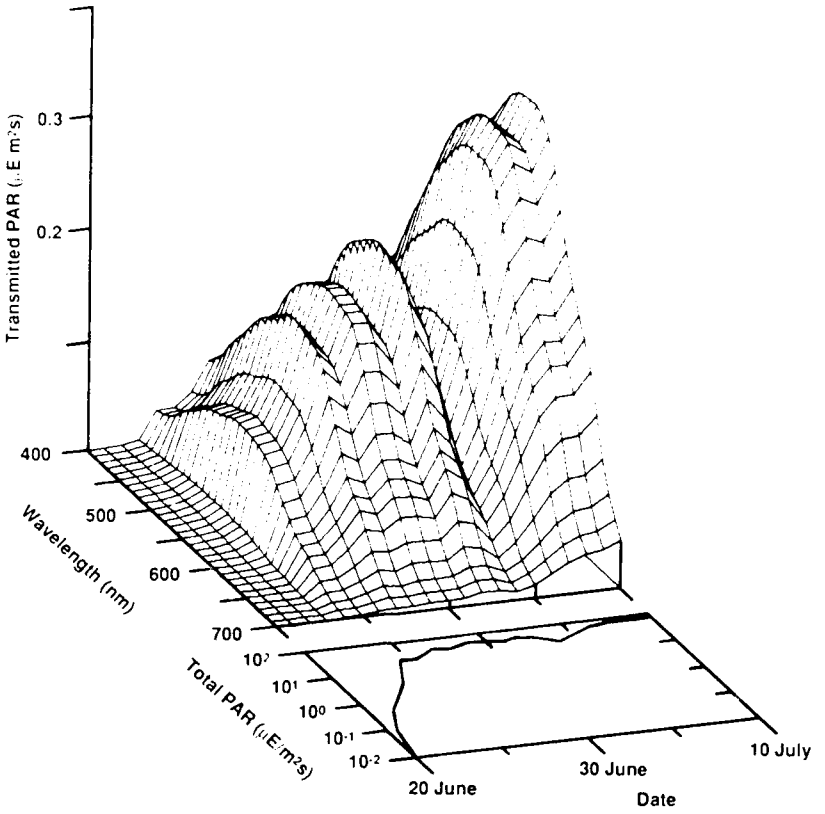

Figure 10. Temporal evolution of spectral and total PAR for the Mould Bay ice cover. Units of PAR are µE/m² s.

2 (dashed line) remained constant during the experiment and this was reflected in an albedo that was temporally invariant. Site 1 (shaded envelope) exhibited a very slight decrease with time due to the thinning of the snow cover. Changes in spectral albedo were most dramatic at site 3, where surface conditions evolved from cold dry snow, to melting snow, to bare white ice, to melting blue ice, to a melt pond with a corresponding continual decrease in albedo. Daily albedos at site 3 from 20 June to 7 July are represented by the family of curves in Figure 11.

Transmitted values of total PAR for the three sites are presented in Figure 12. Total transmitted PAR integrated over the 18-day period was 17.6 µE/m²s for site 1, 12.6 for site 2, and 31.6 for site 3. Values at sites 1 and 3 were small initially, but increased as the snow cover melted. Transmitted PAR was the greatest at site 3 after the snow melted and a melt pond formed. At site 2 results were fairly constant during the entire observation period. There was a sharp increase in total transmitted PAR at site 1 between 6 and 7 July as the snow thickness decreased from 0.10 to 0.04 m. On 20 June site 2 had the highest transmission, yet by the end of the experiment

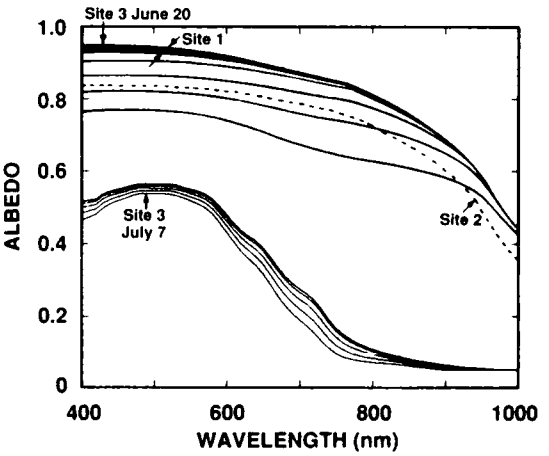

Figure 11. Spectral albedos from sites 1, 2, and 3. The shaded area represents albedos for site 1, the dashed line shows the albedo at site 2, and the series of curves depicts daily albedos at site 3 from 20 June (high) to 7 July (low)

Table 3. Environmental conditions for MIZEX 84 sites.

Date (1984)	Cloud conditions	Incident shortwave (W/m^2)	Snow (s) and ice (i) thickness (m) Site 1 H_s	Site 1 H_i	Site 2 H_s	Site 2 H_i	Site 3 H_s	Site 3 H_i
20 June	Clear skies	300	0.38	2.02	0.00	3.87	0.21	3.32
21 June	Clear skies	305	0.34	2.01	0.00	3.83	0.18	3.29
22 June	Light clouds, solar disk visible	215	0.32	2.01	0.00	3.82	0.16	3.28
23 June	Light clouds, solar disk visible	220	0.29	2.00	0.00	3.79	0.15	3.27
24 June	Clear skies	277	0.28	1.98	0.00	3.79	0.14	3.26
25 June	Cloudy, solar disk barely visible	183	0.27	1.96	0.00	3.78	0.14	3.25
26 June	Cloudy, solar disk barely visible	194	0.25	1.92	0.00	3.76	0.11	3.25
27 June	Cloudy, solar disk barely visible	172	0.24	1.85	0.00	3.74	0.11	3.22
28 June	Cloudy, solar disk barely visible	171	0.24	1.83	0.00	3.73	0.10	3.20
29 June	Cloudy, solar disk barely visible	159	0.23	1.79	0.00	3.69	0.06	3.16
30 June	Cloudy, solar disk barely visible	168	0.19	1.76	0.00	3.65	0.03	3.13
1 July	Heavy overcast, solar disk not visible	114	0.17	1.71	0.00	3.60	0.02	3.11
2 July	Cloudy, solar disk barely visible	170	0.16	1.68	0.00	3.59	0.01	3.10
3 July	Cloudy, solar disk barely visible	157	0.15	1.67	0.00	3.57	0.00	3.06*
4 July	Heavy overcast, solar disk not visible	136	0.13	1.65	0.00	3.54	0.00	3.00
5 July	Heavy overcast, solar disk not visible	137	0.11	1.62	0.00	3.49	0.00	2.91
6 July	Heavy overcast, solar disk not visible	104	0.10	1.60	0.00	3.40	0.00	2.78
7 July	Heavy overcast solar disk not visible	100	0.04	1.60	0.00	3.23	0.00	2.64

* H_i for site 3 designates the formation of a melt pond.

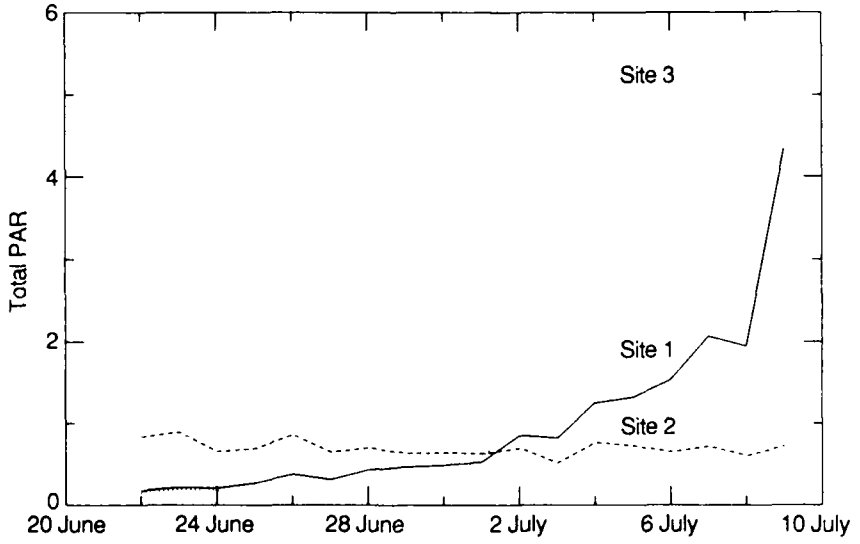

Figure 12. Total PAR ($\mu E/m^2s$) as a function of time for sites 1, 2, and 3.

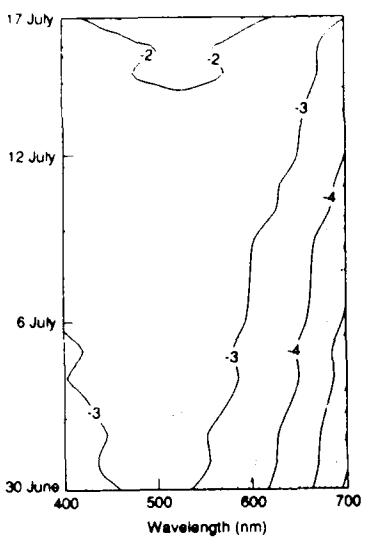

a. Site 1.

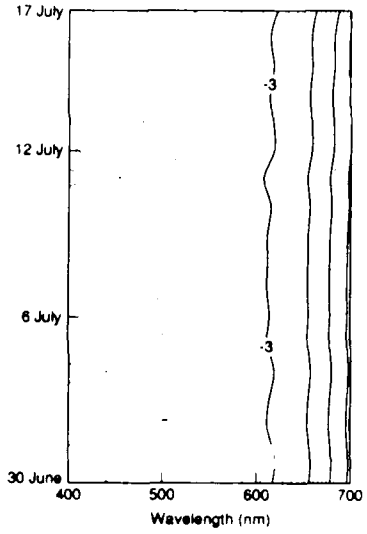

b. Site 2.

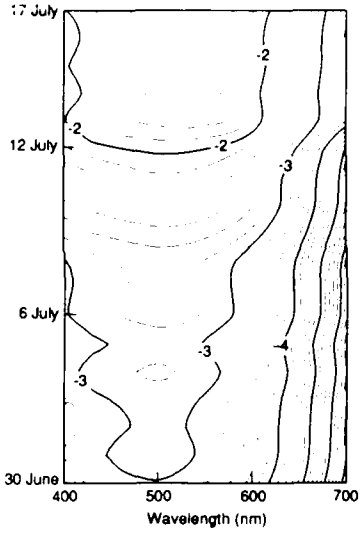

c. Site 3.

Figure 13. Contours of spectral PAR for sites 1, 2, and 3. The contours represent orders of magnitude of spectral transmitted PAR (μE/m²s), for example the –2 contour denotes a PAR of 10^{-2} μE/m²s. The contour interval is 0.2.

it was the lowest. In fact, readings at site 3 increased from 20% of site 2 to 500% of site 2. Even over this small 5-m spatial scale, at a particular time, differences in transmitted PAR between the three sites were as large as a factor of five, illustrating the potential inaccuracies of estimating transmitted PAR from a single set of measurements.

Transmitted PAR as a function of time and wavelength for sites 1, 2, and 3 are plotted in Figure 13. The contours are isopleths of the base 10 logarithm of transmitted PAR (0.2 intervals). The sharp dropoff of PAR at wavelengths beyond 650 nm is evident in all three cases. Maximum PAR is transmitted between 450 and 550 nm. Temporal changes were greatest at site 3, with an increase in PAR at 470 nm of one and a half orders of magnitude. In essence the formation of the melt pond at site 3 is analogous to opening a window in the ice cover.

DISCUSSION

A sea ice cover can have tremendous variability in the reflected and transmitted radiation fields. On a single floe ice thickness can vary from centimeter-thick nilas to ridges tens of meters thick, while snow depths can range from zero to a meter or more. Over horizontal distances of a few meters surface conditions can change from snow-covered ice to bare white ice to ponded ice. As we have seen in the three case studies, this can result in values of light transmittance that vary by several orders of magnitude. Temporal evolution during the melt cycle is also quite significant. Removal of the snow cover results in a reduction in albedo and a sharp increase in transmittance. The formation of melt ponds causes a further decrease in albedo and enhancement of transmittance.

This complexity makes estimation of areally or temporally averaged values of reflected or transmitted light difficult. However, such values are important for a number of applications, including assessments of biological activity, internal ice melting, and regional albedos. Single point measurements of albedo or transmittance are inadequate to define areal averages, while measurements on a detailed spatial scale are not practical.

The model presented in this report provides a mechanism for estimating light reflection and transmission for such complex ice covers. Because of the model's computational simplicity, the optical properties of an ice cover can be represented in spatial or temporal detail. The input parameters needed for the computation are all easily observable quantities: ice thickness, snow depth, ice surface conditions, and a qualitative description of the medium's composition in terms of ice and snow types. Once the structural description is specified, the model enables spectral albedos, PAR values, and transmittances to be calculated.

Currently the model is limited to nine snow and ice types. While these types constitute a considerable collection, there are a few significant omissions. For example, there is a scarcity of data on the optical properties of antarctic pack ice. Because of the significant biological activity within and beneath the antarctic ice cover, this is a region of extreme interest for optical modeling. Structurally antarctic sea ice is quite different from arctic ice (Gow et al.1982), with large expanses of pancake ice and a preponderance of frazil rather than columnar crystals. This difference in ice structure presumably results in some disparity in optical properties. The presence of contaminants in the ice, such as biological organisms, would also change its optical properties. Measurements are needed to determine spectral scattering and extinction coefficients for these ice types to extend the model to these cases.

LITERATURE CITED

Bohren, C.F. and Huffman, D.R. (1983) *Absorption and Scattering of Light by Small Particles*, New York: Wiley.

Chandrasekhar, S.C. (1960) *Radiative Transfer*. New York: Dover.

Dunkle, R.V. and J.T. Bevans (1956) An approximate analysis of the solar reflectance and transmittance of a snow cover. *Journal of Meteorology*, **13:** (20): 212–216.

Gast, P.R. (1960) Solar radiation. *Handbook of Geophysics* (C.F Campen et al., Ed.). New York: MacMillan.

Gow, A.J., S.F. Ackley, W.F. Weeks and J,.W. Govoni (1979) Physical and structural characteristics of antarctic sea ice. *Annals of Glaciology*, **3:** 113–117.

Grenfell, T.C. (1979) The effects of ice thickness on the exchange of solar radiation over the polar oceans. *Journal of Glaciology*, **22**(87): 305–320.

Grenfell, T.C. (1983) A theoretical model of the optical properties of sea ice in the visible and near infrared. *Journal of Geophysical Research*, **88**(C11): 9723–9735.

Grenfell, T.C. and G.A. Maykut (1977)The optical properties of ice and snow in the Arctic Basin. *Journal of Glaciology*, **18:** 445–463.

Grenfell, T.C. and D.K. Perovich (1981) Radiation absorption coefficients of polycrystalline ice from 400–1400 nm. *Journal of Geophysical Research*, **86:** 7447–7450.

Grenfell, T.C. and D.K. Perovich, (1984) Spectral albedos of sea ice and incident solar irradiance in the Southern Beaufort Sea. *Journal of Geophysical Research*, **89:** 3573–3580.

Maykut, G.A. and N.U. Untersteiner (1971) Some results from a time dependent, thermodynamic model of sea ice.*Journal of Geophysical Research*, **76**(6): 1550–1575.

Maykut, G.A. and D.K. Perovich (1985) MIZEX 84 heat and mass balance data. APL-UW 12-85, Applied Physics Laboratory, University of Washington, Seattle.

Maykut, G.A. and D.K. Perovich (1987) The role of shortwave radiation in the summer decay of a sea ice cover. *Journal of Geophysical Research*, **92**(C5): 7032–7044.

Mullen, P.C. and S.G.Warren (1988) Theory of the optical properties of lake ice. *Journal of Geophysical Research*, **93**(D7): 84038414.

Perovich, D.K. (1979) The optical properties of young sea ice. M.S. thesis (unpublished), University of Washington, Seattle.

Perovich, D.K. (1983) On the summer decay of a sea ice cover. Ph. D dissertation (unpublished) University of Washington, Seattle.
Perovich, D.K. and T.C.,Grenfell (1981) Laboratory studies of the optical properties of young sea ice.*Journal of Glaciology*, **27:** 331–346.
Perovich, D.K. and T.C. Grenfell (1982) A theoretical model of radiative transfer in young sea ice. *Journal of Glaciology*, **28**(99): 341–356.
Perovich, D.K. G.A. Maykut, and T.C.Grenfell (1986) Optical properties of ice and snow in the polar oceans. I: Observations. *Society of Photo-Optical Instrumentation Engineers Technical Symposium Southeast on Optical and Optoelectronic Systems, 31 March–2 April 1986, Orlando, Florida*, SPIE Proceedings vol. 637.
Schuster, A. (1905) Radiation through a foggy atmosphere. *Astrophysical Journal*, **21**(1): 1–22.
SooHoo, T.B., A.C. Palmisano, S.T. Kottmeier, M.P. Lizotte, S.L. SooHoo and C.L. Sullivan (1987) Spectral light absorption and quantum yield of photosynthesis in sea ice microalgae and a bloom of *Phaeocystis pouchettii* from McMurdo Sound, Antarctica. *Marine Ecology*, **33:** 175–189.
Smith, R.C. and K.S. Baker (1981) Absorption coefficients of the clearest natural waters. *Applied Optics*, **20:** 177–184.
Warren, S.G. (1982) Optical properties of snow. *Review of Geophysics and Space Physics*, **20**(1): 67–89.
Wiscombe, W.J. and Warren, S.G. (1980) A model for spectral albedos of snow. 1: Pure snow, *Journal of Atmospheric Science*, **37:** 2712–2733.

APPENDIX A: DECOUPLING OF FIRST-ORDER DIFFERENTIAL EQUATIONS

The upwelling and downwelling irradiances are defined by the coupled differential equations

$$dF_{\downarrow}(z,\lambda) = -k_{\lambda}F_{\downarrow}(z,\lambda)dz - r_{\lambda}F_{\downarrow}(z,\lambda)dz + r_{\lambda}F_{\uparrow}(z,\lambda)dz \quad \text{(A1)}$$

$$dF_{\uparrow}(z,\lambda) = k_{\lambda}F_{\uparrow}(z,\lambda)dz - r_{\lambda}F_{\downarrow}(z,\lambda)dz + r_{\lambda}F_{\uparrow}(z,\lambda)dz \quad \text{(A2)}$$

In order to solve for $F_{\downarrow}(z,\lambda$ and $F_{\uparrow}(z,\lambda)$ these equations are reformulated as uncoupled second order equations. Equations A1 and A2 can be rewritten as

$$(d/dz + k_{\lambda} + r_{\lambda})\, F_{\downarrow}(z,\lambda) - r_{\lambda}F_{\uparrow}(z,\lambda) = 0 \quad \text{(A3)}$$

$$r_{\lambda}F_{\downarrow}(z,\lambda) + (d/dz - k_{\lambda} - r_{\lambda})\, F_{\uparrow}(z,\lambda) = 0 \quad \text{(A4)}$$

respectively. Operate on eq A3 by multiplying by (r_{λ}):

$$r_{\lambda}(d/dz + k_{\lambda} + r_{\lambda})F_{\downarrow}(z,\lambda) - r_{\lambda}^{2}F_{\uparrow}(z,\lambda) = 0. \quad \text{(A5)}$$

Operate on eq A4 with $(d/dz + k_{\lambda} + r_{\lambda})$:

$$(d/dz + k_{\lambda} + r_{\lambda})r_{\lambda}\, F_{\downarrow}(z,\lambda) + (d/dz + k_{\lambda} + r_{\lambda})\, [d/dz - (k_{\lambda} + r_{\lambda})]\, F_{\uparrow}(z,\lambda) = 0. \quad \text{(A6)}$$

Subtracting eq A5 from A6 gives

$$(d^{2}/dz^{2})F_{\uparrow}(z,\lambda) - (k_{\lambda}^{2} + 2k_{\lambda}r_{\lambda})F_{\uparrow}(z,\lambda) = 0, \quad \text{(A7)}$$

which has the solution

$$F_{\uparrow}(z,\lambda) = C\sinh(\kappa_{\lambda}z) + D\cosh(\kappa_{\lambda}z). \quad \text{(A8)}$$

An equation for $F_{\downarrow}(z,\lambda)$ is determined in a similar fashion. Equation A3 is operated on with

$$(d/dz - k_{\lambda} - r_{\lambda})$$

and eq A4 is multiplied by r_{λ} giving

$$(d/dz - k_{\lambda} - r_{\lambda})(d/dz + k_{\lambda} + r_{\lambda})\, F_{\downarrow}(z,\lambda) - (d/dz - k_{\lambda} - r_{\lambda})\, r_{\lambda}F_{\uparrow}(z,\lambda) = 0 \quad \text{(A9)}$$

and

$$r_{\lambda}^{2}F_{\downarrow}(z,\lambda) + (d/dz - k_{\lambda} - r_{\lambda})\, r_{\lambda}F_{\uparrow}(z,\lambda) = 0. \quad \text{(A10)}$$

Adding eq A9 and A10 gives

$$(d^{2}/dz^{2})\, F_{\downarrow}(z,\lambda) - (k_{\lambda} + r_{\lambda})\, (k_{\lambda}^{2} + 2k_{\lambda}r_{\lambda})F_{\downarrow}(z,\lambda) = 0, \quad \text{(A11)}$$

which has the solution

$$F_{\downarrow}(z,\lambda) = A\sinh(\kappa_{\lambda}z) + B\cosh(\kappa_{\lambda}z). \quad \text{(A12)}$$

Equations A8 and A12 can also be expressed in terms of $\exp(\kappa_{\lambda}z)$ and $\exp[-(\kappa_{\lambda}z)]$. A solution using $\sinh(\kappa_{\lambda}z)$ and $\cosh(\kappa_{\lambda}z)$ was selected because it gave greater numerical stability when inverting the matrix defined in Figure 2.

A facsimile catalog card in Library of Congress MARC format is reproduced below.

Perovich, Donald K.

A two-stream, multilayer, spectral radiative transfer model for sea ice / by Donald K. Perovich. Hanover, N.H.: U.S. Army Cold Regions Research and Engineering Laboratory; Springfield, Va.: available from National Technical Information Service, 1989.

iii, 20 p., illus., 28 cm. (CRREL Report 89-15.)

Bibliography: p. 15.

1. Albedo. 2. Arctic. 3. Radiative transfer. 4. Sea ice. 5. Shortwave radiation. I. United States Army. II. Corps of Engineers. III. Cold Regions Research and Engineering Laboratory. V. Series: CRREL Report 89-15.

END

FILMED

10-89

DTIC